Revealing the Epitaxial Interface between Al13Fe4 and Al5Fe2 Enabling Atomic Al Interdiffusion

Corentin Chatelier, Kanika Anand, Peter Gille, Marie-Cécile de Weerd, Julian Ledieu, Vincent Fournée, Andrea Resta, Alina Vlad, Yves Garreau, Alessandro Coati, et al.

Revealing the epitaxial interface between $Al_{13}Fe_4$ and Al_5Fe_2 enabling atomic Al interdiffusion

Corentin Chatelier,[1,2] Kanika Anand,[1] Peter Gille,[3] Marie-Cécile De Weerd,[1] Julian Ledieu,[1] Vincent Fournée,[1] Andrea Resta,[2] Alina Vlad,[2] Yves Garreau,[2,4] Alessandro Coati[2,*] and Émilie Gaudry[1,*]

[1] *Univ. Lorraine, CNRS, Institut Jean Lamour, 2 allé André Guinier, 54000 Nancy, France*
[2] *Synchrotron SOLEIL, L'Orme des Merisiers, Départementale 128, 91190 Saint-Aubin, Gif-sur-Yvette Cedex, France*
[3] *Ludwig-Maximilians-Univ., Geschwister-Scholl-Platz 1, D-80539 München, Germany*
[4] *Univ. Paris-Cité, CNRS, Matériaux et Phénomènes Quantiques Paris, Bâtiment Condorcet, 10 rue Alice Domon et Léonie Duquet, Case courrier 7021, F-75205 Paris Cedex 13, France*

E-mail: emilie.gaudry@univ-lorraine.fr,alessandro.coati@synchrotron-soleil.fr

Abstract

Steel is the most commonly manufactured materials in the world. Its performances can be improved by hot-dip coating with the low weight aluminium metal. The structure of the Al||Fe interface, which is known to contain a buffer layer made of complex intermetallic compounds such as Al_5Fe_2 and $Al_{13}Fe_4$, is crucial for the properties. On the basis of surface X-ray diffraction, combined with theoretical calculations, we derive in this work a consistent model at the atomic scale for the complex $Al_{13}Fe_4(010)||Al_5Fe_2(001)$ interface. The epitaxial relationships are found to be $[130]_{Al_5Fe_2} \parallel [010]_{Al_{13}Fe_4}$ and $[1\bar{1}0]_{Al_5Fe_2} \parallel [100]_{Al_{13}Fe_4}$. Interfacial and constrained energies, as well as works of adhesion, calculated for several structural models based on Density Functional Theory, identify the lattice mismatch and the interfacial chemical composition as main factors for the stability of the interface. Molecular dynamics simulations suggest a mechanism of Al diffusion, to explain the formation of the complex $Al_{13}Fe_4$ and Al_5Fe_2 phases at the Al||Fe interface.

KEYWORDS: Surface X-Ray Diffraction, Density Functional Theory, Al-Fe Interface, Adhesion, $Al_{13}Fe_4$, Al_5Fe_2

Introduction

Interfaces are known to play an important role in a broad range of scientific and technological fields, such as catalysis,[1–3] electronics,[4,5] or coatings.[6,7] Their design is crucial to improve the performances of heterostructures, as demonstrated in numerous studies, involving metallic, semiconductor or insulating buffers.

Advanced properties are generally obtained by combining two systems with dissimilar characteristics. In metallurgy, aluminized steel combines the low weight of aluminium with the high strength of steel. This low-cost material shows a better corrosion resistance than most metals, as well as excellent high-temperature performances and heat reflectivity, enabling its use in a wide range of applications.[8] But the distinct thermal and physical properties of Al and Fe metals make it challenging to join. Buffer layers generally forms at the interface, made of Al-Fe intermetallic compounds. Their compositions depend on the chemical potentials, the nucleation conditions and the mobilities of the elements.[9] They can significantly reduce the mechanical properties of the heterostructure and limit the durability.[10] Thus, controlling this buffer layer is crucial.[11]

Several phases can be observed at the interface between fcc Al and bcc Fe : Al_6Fe, $Al_{13}Fe_4$, Al_2Fe, Al_5Fe_2, AlFe, $AlFe_3$.[12,13] Among them, Al_5Fe_2 and $Al_{13}Fe_4$ are known to be frequently formed, as they nucleate almost spontaneously.[14–16] Due to the low solubility limit (0.012% at 550^{o}C)[17] and low diffusion coefficient of iron in aluminium (D=8.76×10^{-11} cm^2/s at 550^{o}C),[18] the complex $Al_{13}Fe_4$ phase is known to first form at the Al||Fe interface, which subsequently decomposes into Al_5Fe_2 at the Fe||$Al_{13}Fe_4$ interface. A distribution of morphologies and sizes is observed for Al_5Fe_2 by electron microscopy, but with a preferred growth direction – parallel to the normal direction of the (001) plane.[19] Depending on the reaction conditions, the growth kinetics of Al_5Fe_2 can be described by parabolic rate laws, while the thickness of the $Al_{13}Fe_4$ layer does not expand significantly.[20]

Further understanding of the growth process and the mechanical properties of the join require the knowledge of the atomic arrangements at the interface. Experimental methods, like electron microscopy or X-ray diffraction, identified the microstructure and the nature of the phases. Based on High resolution transmission electron microscopy (HRTEM) the epitaxial relationships have been suggested to be:[21]

$$[2\bar{2}1]_{Al_{13}Fe_4}\|[0\bar{1}1]_{Al},(330)_{Al_{13}Fe_4}\|(200)_{Al} \quad (1)$$

$$[0\bar{1}0]_{Al_{13}Fe_4}\|[0\bar{1}0]_{Al_5Fe_2},(204)_{Al_{13}Fe_4}\|(202)_{Al_5Fe_2} \quad (2)$$

$$[5\bar{3}\bar{1}0]_{Al_5Fe_2}\|[0\bar{1}1]_{Fe},(15\bar{1})_{Al_5Fe_2}\|(011)_{Fe} \quad (3)$$

The previous relationships imply rather large lattice mismatches ($\simeq$ 3.5% for $Al_{13}Fe_4$||Al_5Fe_2 and Al_5Fe_2||Fe, Eqs. 2,3), especially for Al||$Al_{13}Fe_4$ (Eq. 1, 9.8%). The preferred orientation, observed for Al_5Fe_2 at the interface (parallel to the $[001]_{Al_5Fe_2}$ direction),[19] is not found here. In addition, the proposed Miller indexes are not those of dense planes, which suggests the presence of low stability interfacial layers.

On the theoretical side, the structural and mechanical properties of Al-Fe phases have been extensively calculated, using empirical potentials[22–25] or DFT methods.[26–28] A few studies also focused on interfaces. Molecular dynamics investigated the fcc Al(111)||bcc Fe(110) system, and identified misfit dislocations in the aluminium region. But only the FeAl 1:1 compound is found to form at the interface, and complex phases such as $Al_{13}Fe_4$ and Al_5Fe_2, are not observed in the simulations.[29] DFT calculations have systematically modeled the Al||Fe, Al||$Al_{13}Fe_4$, $Al_{13}Fe_4$||Al_5Fe_2 and Al_5Fe_2||Fe interfaces.[30–32] Structural models have been build based on automated structure-searching methods to determine the possible lattice matches between two arbitrary surfaces.[33] But

the considered epitaxial relationships are not those found experimentally.

On the basis of surface X-ray diffraction (SXRD), combined with DFT calculations, we derive in this work a consistent model at the atomic scale for the complex $Al_{13}Fe_4||Al_5Fe_2$ interface. Ab initio calculations of interfacial energies, adhesion energies and constrained energies, using several structural models, identify the lattice mismatch and the chemical composition at the interface as main factors for the stability. Molecular dynamic simulations suggest a mechanism of Al diffusion to explain the formation of the complex $Al_{13}Fe_4$ and Al_5Fe_2 phases at the interface.

Results and discussion

The monoclinic $Al_{13}Fe_4$ and the orthorhombic Al_5Fe_2 compounds both belong to the family of complex intermetallics. They crystallize in two distinct space groups : C2/m (12, mS102)[34] and Cmcm (63, oS15)[35–37] for $Al_{13}Fe_4$ and Al_5Fe_2, respectively, with quite different cell parameters (Figs. 1-2)[34,36] :

$$\begin{aligned} a^{lit.}_{Al_{13}Fe_4} &= 15.49\ \text{Å} \\ b^{lit.}_{Al_{13}Fe_4} &= 8.08\ \text{Å} \\ c^{lit.}_{Al_{13}Fe_4} &= 12.47\ \text{Å} \\ \beta^{lit.}_{Al_{13}Fe_4} &= 107.69^{o} \end{aligned}$$

and

$$\begin{aligned} a^{lit.}_{Al_5Fe_2} &= 7.66\ \text{Å} \\ b^{lit.}_{Al_5Fe_2} &= 6.39\ \text{Å} \\ c^{lit.}_{Al_5Fe_2} &= 4.19\ \text{Å} \end{aligned}$$

These two phases share similarities in their local atomic structure, described in both cases by a stacking of planes (Fig. 1(c,d) and Fig.2b). The 102 atoms in the $Al_{13}Fe_4$ crystal cell are distributed over four atomic planes perpendicular to the pseudo-10fold direction ([010]), with the sequence $F_0P_{0.25}F_{0.5}P_{0.75}$, where indices indicates the mean position of each plane along the [010] axis, using reduced coordinates. Dense atomic planes of the Al_5Fe_2 phase lie perpendicular to the [001] direction. Pentagonal atomic arrangements are found in both compounds (Fig. 1(a,d) and Fig. 2a). In $Al_{13}Fe_4$, individual Fe-centered Al pentagon corresponds to either the bottom or the top cap of the pentagonal bipyramid clusters suggested to describe geometrically the bulk structure.[34,38,39] In the case of Al_5Fe_2, rigid pentagonal antiprisms, made of fully occupied Fe and Al_1 sites, form channels extending along the [001] direction. Disordered chains made of partially occupied Al sites are confined within the channels. The easy diffusion of Al within the channels, quantified by their low migration energy barrier (0.7 eV, calc. value),[26] i.e. of the same order of magnitude than that for a self-diffusion of Al in a fcc lattice (0.65 eV, exp. value),[40] is ascribed to their curved migration path and the large concentration of Al vacancies within the channels.[26]

It is believed that the previous diffusion process is involved in the formation of the thin layer of $Al_{13}Fe_4$ at the interface formed during hot dip aluminizing of mild steel. Indeed, the dipping interface consist of a thick layer of Al_5Fe_2 (4.2-132.2 μm) next to the steel and a thin layer of $Al_{13}Fe_4$ (less than 5.5 μm) next to the aluminium coating.[20] In this work, the interface between $Al_{13}Fe_4$ and Al_5Fe_2 is formed during the surface preparation of $Al_{13}Fe_4(010)$, i.e. over the sputtering/annealing cycles carried out under ultra-high vacuum conditions (see section Method for details).

The interface is first investigated by SXRD. Figures 3 and S1 show the in-plane map of the $Al_{13}Fe_4(010)$ reciprocal space (extinction conditions are $K + L = 2n + 1$ with $n \in \mathbb{N}$). The two series of diffraction spots, indicated with red and black circles (Figs. 3 and S1), support the existence of two domains in the sample, in agreement with the LEED pattern (Fig. S4). The observed pseudo 10-fold symmetry

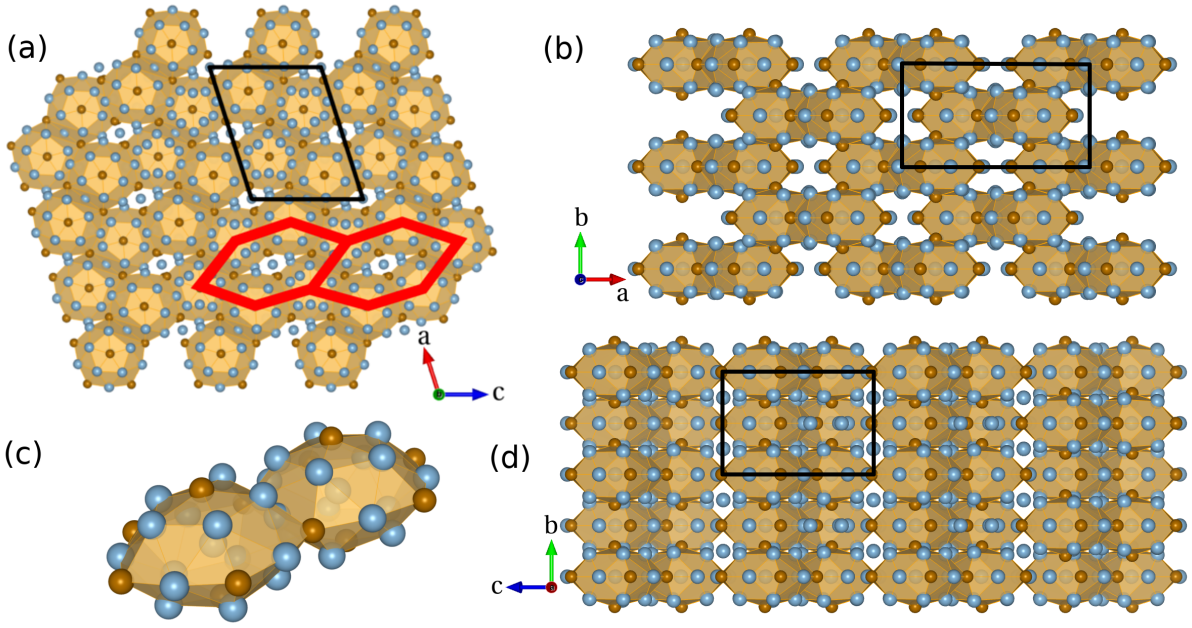

Figure 1: Bulk structure of $Al_{13}Fe_4$: (a) along $[010]_{lit.}$ (the hexagonal clusters are drawn in red), (b) along $[001]_{lit.}$, (c) perspective view to show two AlFe Henley-type clusters and (d) along $[100]_{lit.}$. Al and Fe atoms are drawn in light blue and dark orange, respectively.

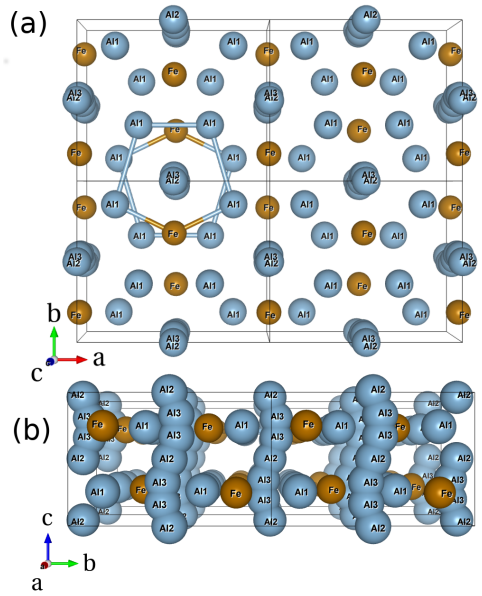

Figure 2: Bulk structure of Al_5Fe_2 : (a) along $[001]_{lit.}$, showing the pentagonal structures made of Al_1 and Fe atoms, (b) along $[100]_{lit.}$, showing the distorted chains of Al_2 and Al_3 atoms. Al and Fe atoms are drawn in light blue and dark orange, respectively.

confirms the (010) surface orientation. The lattice parameters deduced from SXRD are consistent with the ones given by the literature (the c axis is normal to the surface according to SXRD, and thus, the lattice orientation differs from the one of the literature) :

$$\begin{aligned} a^{SXRD}_{Al_{13}Fe_4} &= 12.48(6)\text{Å} \simeq c^{lit.}_{Al_{13}Fe_4} \\ b^{SXRD}_{Al_{13}Fe_4} &= 15.53(3)\text{Å} \simeq a^{lit.}_{Al_{13}Fe_4} \\ c^{SXRD}_{Al_{13}Fe_4} &= 8.10(3)\text{Å} \simeq b^{lit.}_{Al_{13}Fe_4} \end{aligned}$$

The SXRD experiments also identified the Al_5Fe_2 phase, through the measured lattice parameters :

$$\begin{aligned} a^{SXRD}_{Al_5Fe_2} &= 7.66(1)\text{Å} \simeq a^{lit.}_{Al_5Fe_2} \\ b^{SXRD}_{Al_5Fe_2} &= 6.44(2)\text{Å} \simeq b^{lit.}_{Al_5Fe_2} \\ c^{SXRD}_{Al_5Fe_2} &= 4.23(1)\text{Å} \simeq c^{lit.}_{Al_5Fe_2} \end{aligned}$$

For each $Al_{13}Fe_4(010)$ twin domain, there is also a $Al_5Fe_2(001)$ related domain who appears to have an epitaxial relationship : the green (respectively yellow) $Al_5Fe_2(001)$ domain is related to the black (respectively red) $Al_{13}Fe_4(010)$ domain (Fig. 3 and S2). In summary, a part of the surface exposes an $Al_5Fe_2(001)$ phase, the rest of the surface

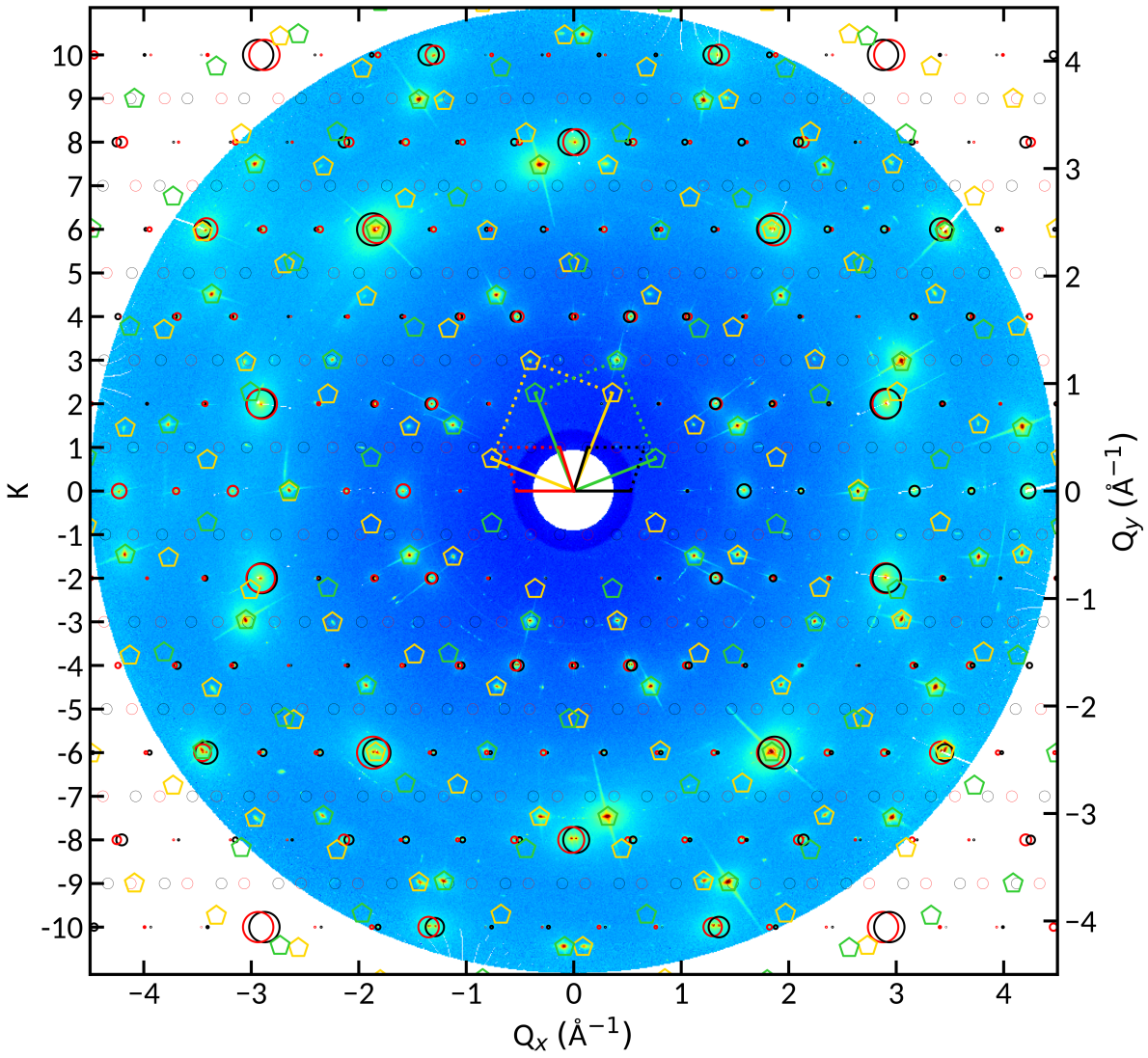

Figure 3: In-plane reciprocal space maps of $Al_{13}Fe_4(010)$. The positions of the $Al_5Fe_2(001)$ spots are shown with yellow and green pentagons. The radii of the circles for $Al_{13}Fe_4(001)$ are proportional to the calculated intensity of the peaks.

area being $Al_{13}Fe_4(010)$. In the following, we assume that the fraction of the surface that exposes $Al_5Fe_2(001)$ is formed on the $Al_{13}Fe_4(010)$ substrate.

For even values of K (K = 2, i.e. $Q_y \simeq 0.8$ Å; K = 4, i.e. $Q_y \simeq 1.6$ Å, etc), the peaks of both twin domains of $Al_{13}Fe_4(010)$ are superimposed, which is an issue for the CTRs measurements because of their difficult deconvolution. Hence, only eight inequivalent CTRs corresponding to odd values of K are considered. Their structure factors are measured for L ranging from 0 to 4.8 (Fig. 4), and compared to the ones calculated using five DFT-relaxed surface models for $Al_{13}Fe_4(010)$ (Fig. 5). According to previous studies,[41,42] the $Al_{13}Fe_4(010)$ topmost layers correspond to incomplete puckered (P) planes present in the bulk crystal structure. The main building block of the corrugated termination consists of two adjacent pentagons of Al atoms, each centered by a protruding Fe atom. These motifs are interconnected via additional Al atoms referred to as *glue* atoms which can desorb. Thus, the five surface models considered in this study are a complete puckered layer (P, Fig. 5), an incomplete puckered layer built from the preservation of the cluster building blocks which also have 2 Al *glue* atoms connecting the bipentag-

onal motifs (P_2^{inc}, Fig. 5), two models where only 1 Al *glue* is missing ($P_{1_a}^{inc}$ and $P_{1_b}^{inc}$, Fig. 5) and finally one model where no Al *glue* is present (P_0^{inc}, Fig. 5). Overall, the incomplete type models are visually better fitting the experimental measurements, see for instance the (1,1) CTR for L ranging from 0 to 2. A χ^2 analysis is yet necessary to discriminate between all the models. Tab. S3 sums up the ROD fitting results, performed with only one fitting parameter (the scale factor). P and $P_{1_b}^{inc}$ models are the worst fitting ones. $P_{1_a}^{inc}$ is overall the best model with a χ^2 value of 4.445 and a R-factor of 0.460. Nevertheless, the discrepancy between $P_{1_a}^{inc}$ and P_2^{inc} or P_0^{inc} is quite low (around 5% for the χ^2 value and 2% for the R-factor) and therefore maybe not significant. A combination of these three models might also lead to a good agreement. This could lead to a partial desorption of Al *glue* atoms due to a too high annealing temperature, as suggested by ref.[41]

To complement the SXRD analysis, surface energy calculations have been performed with the previous five surface models for $Al_{13}Fe_4(010)$ (Fig. 5). Overall, the P_2^{inc} model is the most stable one, with a surface energy ranging from 1.296 J/m^2 to 1.333 J/m^2 The other models (P, $P_{1_a}^{inc}$, $P_{1_b}^{inc}$ and P_0^{inc}) appear to be slightly less stable in the full range of chemical potentials. The two models with only one Al *glue* atom ($P_{1_a}^{inc}$ and $P_{1_b}^{inc}$) present almost the same surface energy in the full range of Al chemical potentials, while P_0 (no Al *glue* atom) is the less stable over the same range of chemical potentials. In summary, the combination of the SXRD analysis and the DFT calculations points to incomplete (P^{inc}-type) models as surface models for $Al_{13}Fe_4(010)$, in agreement with previous works.[41,42] The bulk truncated P model is not likely.

The relative orientation of the two complex phases are also determined by SXRD. We found that the $[010]_{Al_{13}Fe_4}$ and the $[001]_{Al_5Fe_2}$ directions are perpendicular to the interface. It implies that the interface $Al_{13}Fe_4(010)$ and $Al_5Fe_2(001)$ – share pentagonal atomic arrangements. Satellite peaks are present around integer values of $L_{Al_5Fe_2}$ ($\pm$ 0.16) and are likely correlated to the partially occupied sites of the Al disordered chains confined within the pentagonal channels in bulk Al_5Fe_2 (Fig. S3). The splitting of the principal peaks, observed for instance for $L_{Al_5Fe_2} = 2$ and $L_{Al_5Fe_2} = 2.03$, corresponding to a lattice parameter of 4.16(1) Å, could also be linked to the disordered Al chains in Al_5Fe_2. All peaks have been indexed, which implies that no other phase is present.

The $[010]_{Al_{13}Fe_4} \parallel [001]_{Al_5Fe_2}$ interface is further investigated by DFT, using slabs made of 8 atomic layers, i.e. 4 for each phase, topped by a void thickness. These slabs have been built considering that the substrate is either $Al_{13}Fe_4$ or Al_5Fe_2, i.e. with a stretch of either Al_5Fe_2 or $Al_{13}Fe_4$ (Tab. 2). They present two clean surfaces – $Al_5Fe_2(001)$ and $Al_{13}Fe_4(010)$ – and one interface. The surface structure of $Al_5Fe_2(001)$ is a bulk truncated termination with or without ordered Fe vacancies, in agreement with our previous work.[43] The corresponding models are labeled Vac-type and NVac-type models, respectively. The $Al_{13}Fe_4(010)$ surface is built according to the SXRD results presented above, i.e. by an incomplete plane (P_2^{inc}). The interface is modeled based either on the lattice matching algorithm proposed by Zur et al.,[44] implemented in the *MPInterface code* (Sm-, Vac-, NVac-type models, Fig. 7(a,b))[45,46] or on the epitaxial relationship identified by SXRD (Giant model, Fig. 7c and Fig. 6):

$$[130]_{Al_5Fe_2} \parallel [010]_{Al_{13}Fe_4} \quad (4)$$

$$[1\bar{1}0]_{Al_5Fe_2} \parallel [100]_{Al_{13}Fe_4} \quad (5)$$

Each model comes with two prototypes, i.e. a F-type or P-type layer at the interface ($Al_{13}Fe_4$ side), since these two planes alternates in $Al_{13}Fe_4(010)$. The NVac2-2x and Vac2-2x models are built using the $Al_{13}Fe_4$ compound as the substrate (Al_5Fe_2, considered here as the film, is constrained, Tab. 2), while it is the opposite for the NVac4 and Vac4 models

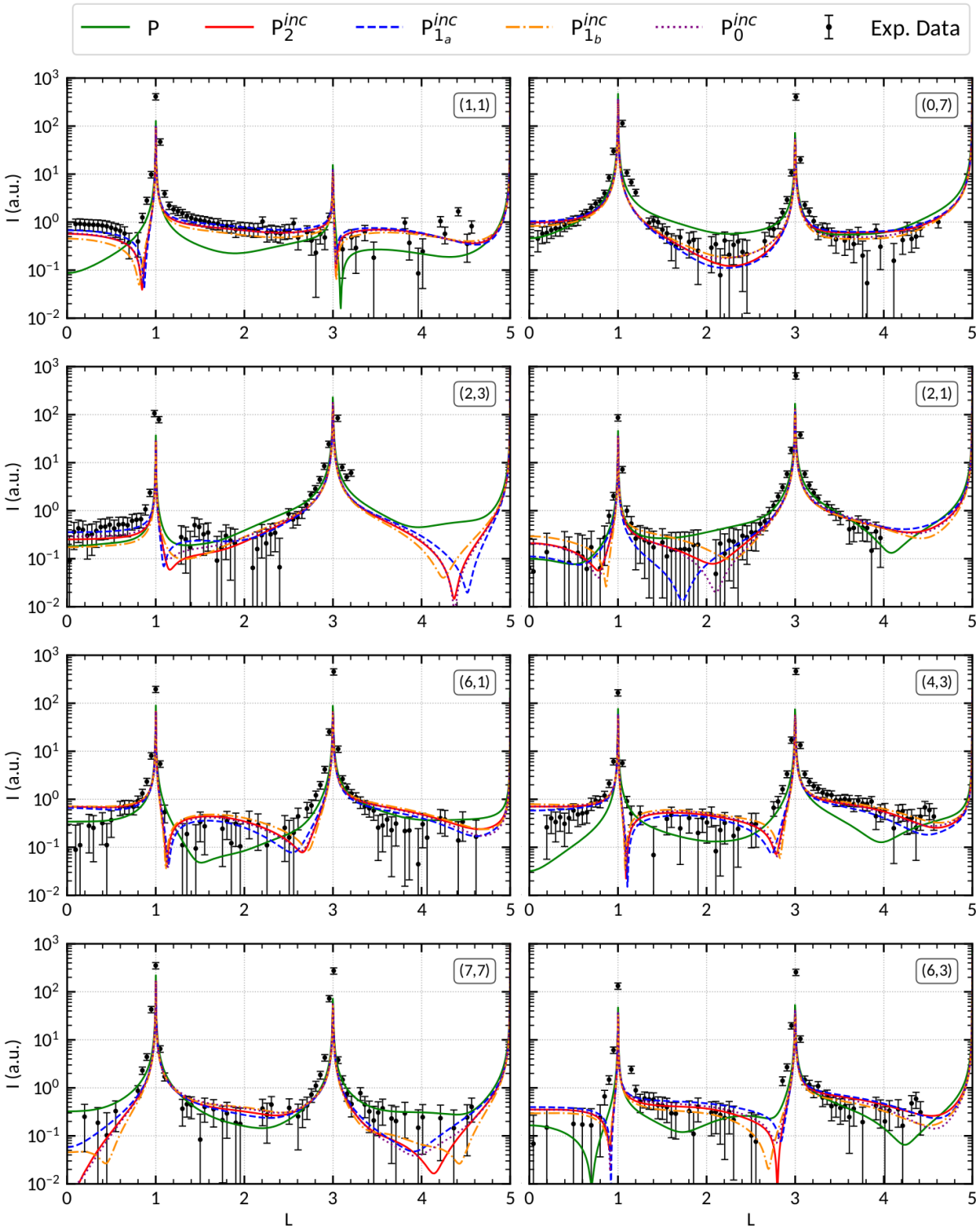

Figure 4: CTRs of $Al_{13}Fe_4(010)$ and their related DFT-based ROD simulation.

(Al_5Fe_2=substrate and $Al_{13}Fe_4$=constrained film, Tab. 2). The epitaxial relationships are illustrated in Fig 7 and detailed in the supporting information. Several smaller models have also been built (Sm-type models, 177≤ N_{atoms} ≤203, Tab. S4). But in the latter cases, the lattice or angle mismatch, calculated with the reference of bulk compounds, is quite large (up to 17 %), and the atomic relaxation leads to the amorphisation of the constrained layer.

A realistic modeling of interfaces requires rather huge slabs to minimize the lattice mis-

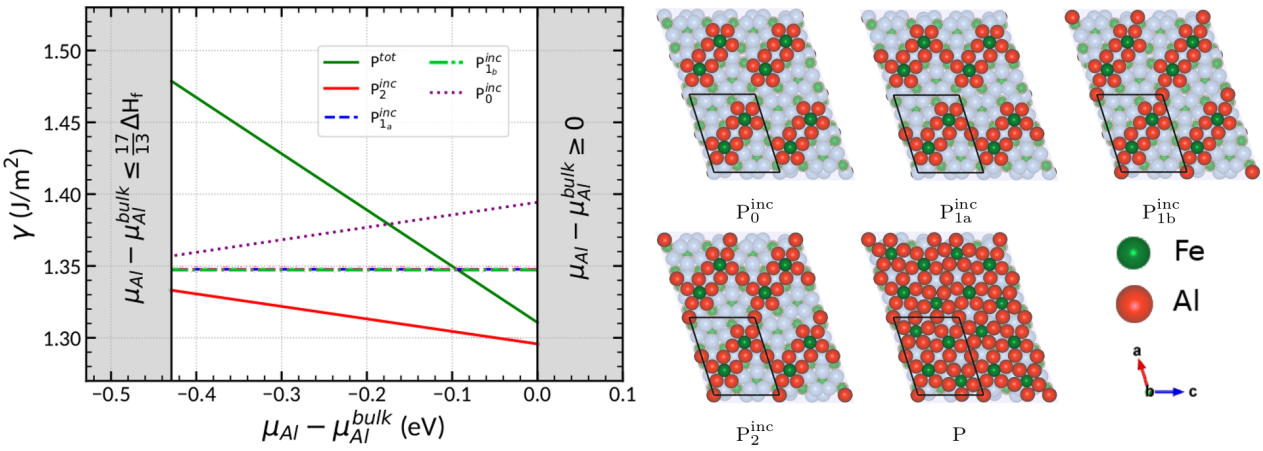

Figure 5: Calculated surface energies of $Al_{13}Fe_4$(010) as a function of the Al chemical potential. The considered surface models for $Al_{13}Fe_4$(010) are detailed on the right-hand side.

match between the two phases in contact. The latter can be reduced to less than 2% by increasing the system size (383≤ N_{atoms} ≤914, Vac- and NVac-type models), and even to less than 1% for the interface built from SXRD results (Tab. 2). In the latter case, the computational box is huge, with 3180 ≤ N_{atoms} ≤3596 (Fig. 6). Simulation boxes with similar sizes have been built using simpler structural models to confirm that size effects do not affect the results (Tabs. S5). The wor of adhesion is rather large for all models (larger than 114.2 meV/Å^2, Tab. 1), and it is maximized for the F-type interface (189.5 and 192.1 meV/Å^2 for the Vac2-2x and Giant models), which may be attributed to the higher content in Fe of this layer.

The interface energy is the lowest for the Giant and the Vac2-2x models, with a value smaller than 10 meV/Å^2 in both cases. However, while the contribution of the constrained energy is also low for the Giant model (-5.5 meV/Å^2) it is quite large for the Vac2-2x model (-177.9 meV/Å^2). It may suggest that the mismatch is not the only parameter that influences the interface energy. It is also supported by the absence of clear correlation between the interface and constrained energies (columns 8 and 9, Tab. 1) calculated for different interfacial layers. Other factors, especially electronic factors, induced by different compositions of the interface, may also play a role.

One noticeable difference between the realistic Vac2-x2 and Giant models comes from the choice of the stretched lattice. In the Giant model, the Al_5Fe_2 cell parameters are almost fixed to their equilibrium value. This leads to a more favorable situation, in agreement with the consideration that Al_5Fe_2 is stiffer, e.g., bulk modulus for Al_5Fe_2 and $Al_{13}Fe_4$ are 127 GPa and 94 GPa, respectively.[47]

Molecular dynamic calculations have been performed to check the behavior of the interface at different temperatures. Two simulation boxes have been built, with the Giant model as structural model for the interface. We started with a thin slab (≃ 36 Å thick, 2×2 surface cell), and we then used a thicker system (≃ 800 Å thick, 50 crystal cells on each side of the interface, 1×1 surface cell). The same simulation scheme has been performed in both cases (see section Methods). It induces rather large modifications at the surfaces (Fig. 9): the protruding Fe atoms at the $Al_{13}Fe_4$(010) termination tend to sink into the surface, and aluminium atoms segregate at the Al_5Fe_2(001) surface, in agreement with the experimental observations.[43] The interface is stable, but rather large structural relaxations are visible within a thin thickness (less than 5 nm, Fig. 8). Aluminium atoms located in the $Al_{13}Fe_4$ phase tend to diffuse to Al_5Fe_2 (inset in Fig. 9), while iron atoms located in the Al_5Fe_2 phase tend to diffuse to $Al_{13}Fe_4$. In addition, Al atoms of the disordered chain in Al_5Fe_2 (in yellow, Fig. 8) are clearly visible in the interfacial region.

This may suggest that the growth of the complex phases at the Al||Fe join indeed involves Al diffusion.

All these simulations have been performed without considering defects such as dislocations, which can drastically impact the mechanical properties at the interface. Nevertheless, our investigation provides important insights about the interface structure at the atomic scale.

Conclusion

In this study, we derived an atomistic model for the $Al_{13}Fe_4(010)$ // $Al_5Fe_2(001)$ interface. On the basis of SXRD, we demonstrate that the epitaxial relationships are

$$[130]_{Al_5Fe_2} \parallel [010]_{Al_{13}Fe_4}$$

$$[1\bar{1}0]_{Al_5Fe_2} \parallel [100]_{Al_{13}Fe_4}$$

which leads to a quite large interfacial cell (2948 $Å^2$). The adhesion, interfacial and constrained energies have been calculated by DFT. The adhesion is rather strong : -208.9 meV/$Å^2$ and -187.9 meV/$Å^2$ for the interfacial F and P atomic layers of $Al_{13}Fe_4$, respectively. It leads to low interfacial energies : 25.9 meV/$Å^2$ and 4.4 meV/$Å^2$, depending on the $Al_{13}Fe_4$ interfacial atomic layer (F vs P). The contribution of the constrained energy is weak : below 15 meV/$Å^2$, attributed to the small lattice mismatch observed for this model (below 1%). Smaller structural models have also been built based on the minimization of the lattice mismatch. They can paint a rather realistic picture of interfacial properties. The lattice mismatch values provide a fair idea of stability (Giant > Vac2-2x > Vac4). In addition, the Vac2-2x leads to adhesion and interfacial energies very similar to the ones of the Giant model, but in this case the mismatch is larger ($\simeq$ 2%), thus leading to larger constrained energies ($\simeq$ 100-200 meV/$Å^2$). Combined with the results obtained for the other interfacial models, this finding suggests that while the lattice mismatch is the main parameter that has an impact on the interfacial energy, electronic factors – here induced by the different compositions of the interface – may also play a role.

The giant model derived by the combination of SXRD and DFT has been further used to investigate the behavior of the interface at different temperatures. Our simulations show that the temperature induces an increase of the thickness of the interfacial region. It also suggests that Al atoms of the $Al_{13}Fe_4$ phase diffuse towards the interface. In situ microbeam surface X-ray scattering would be useful here to probe the growth of the complex intermetallics at the interface, as recently observed for a GaN compound.[48] On the theoretical side, most efficient simulations, based on Monte Carlo methods, may bring more detailed insight into the growth mechanism of the Al//Fe buffer layer at the atomic scale. In any case, this work based on a model system is a first step towards the understanding of polycrystalline Al/Fe interfaces.

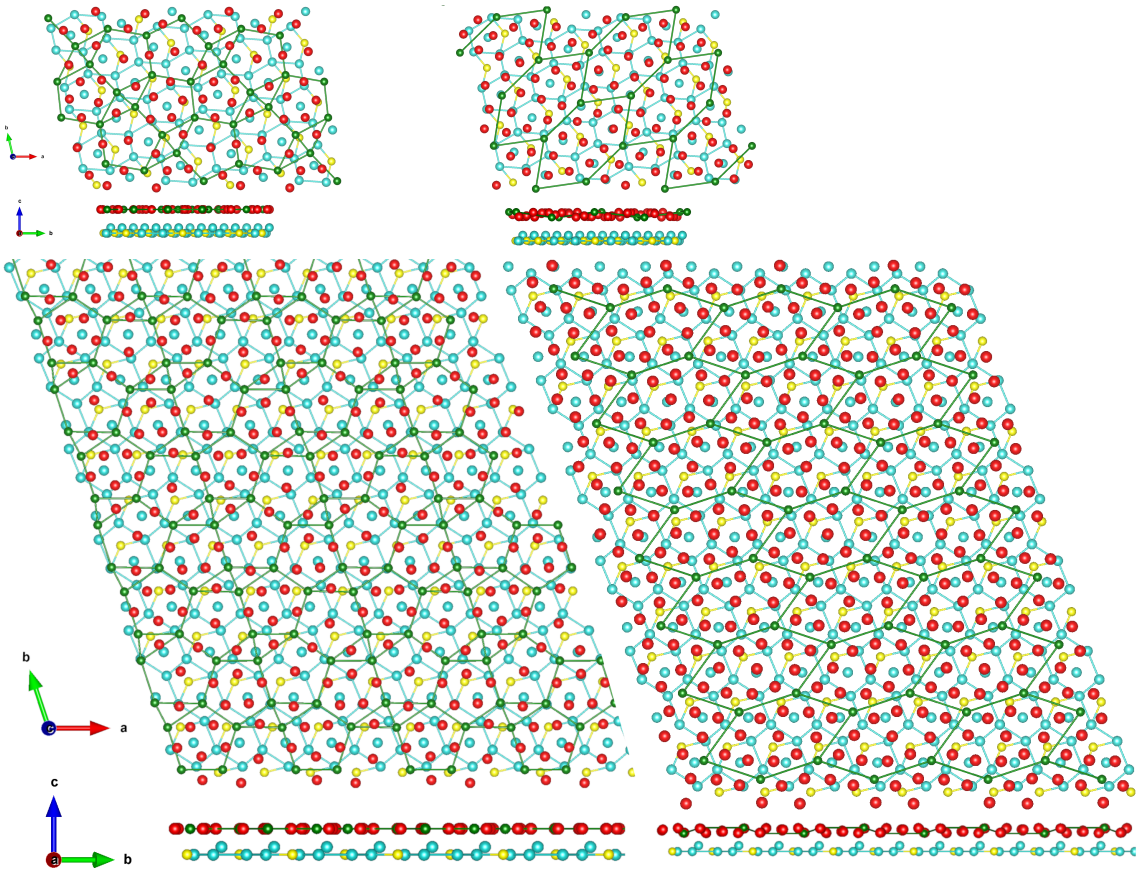

Figure 6: Structure of the Vac2-2x (top) and Giant (bottom) interfacial models. The Al_5Fe_2 phase is depicted by cyan (Al) and yellow (Fe) ; $Al_{13}Fe_4$ phase using red (Al) and green (Fe) spheres. The interface is formed with the F and P layer of $Al_{13}Fe_4(010)$, on the left and right hand side, respectively.

Table 1: Adhesion and interface energies of the Vac2-2x, NVac2-2x, Vac-4, NVac-4 and Giant interface models.

Models		N_{atoms}		Area	W_{adh}	$\gamma_{interface}$	$\Delta E^{constrain}_{Al_{13}Fe_4}$ / $\Delta E^{constrain}_{Al_5Fe_2}$
		$N(Al_5Fe_2)$	$N(Al_{13}Fe_4)$	($Å^2$)	(meV/$Å^2$)	(meV/$Å^2$)	(meV/$Å^2$)
Vac2-2x	F	435	360	730.7	189.5	28.5	-98.1
	P	435	464	730.7	179.7	8.7	-177.9
Vac4	F	203	180	343.9	166.2	51.8	-72.2
	P	203	232	343.9	151.0	37.3	-6.5
NVac2-2x	F	450	360	730.7	156.5	61.5	-79.4
	P	450	464	730.7	146.2	42.1	-149.7
NVac4	F	210	180	343.9	132.1	85.9	-15.4
	P	210	232	343.9	114.2	74.1	-4.8
Giant	F	1740	1440	2947.9	192.1	25.9	-13.7
	P	1740	1856	2947.9	184.0	4.4	-5.5

Table 2: Structural models for the $Al_5Fe_2(001)||Al_{13}Fe_4(010)$ interface.

Models	$Al_{13}Fe_4$		Al_5Fe_2	
	length (Å) / angle (^{o})	strain (%)	length (Å) / angle (^{o})	strain (%)
NVac2-2x, Vac2-2x	a = 15.43	0.0	a = 7.52	1.8
	b = 12.43	0.0	b = 6.48	1.0
	γ = 107.7	0.0	γ = 89.8	0.2
Vac4, NVac4	a = 14.94	-3.2	a = 7.66	0.0
	b = 11.93	-4.0	b = 6.41	0.0
	γ = 105.2	2.3	γ = 90.0	0.0
Giant	a = 15.53	0.7	a = 7.66	0.0
	b = 12.49	0.5	b = 6.41	0.0
	γ = 108.2	0.5	γ = 90	0.0

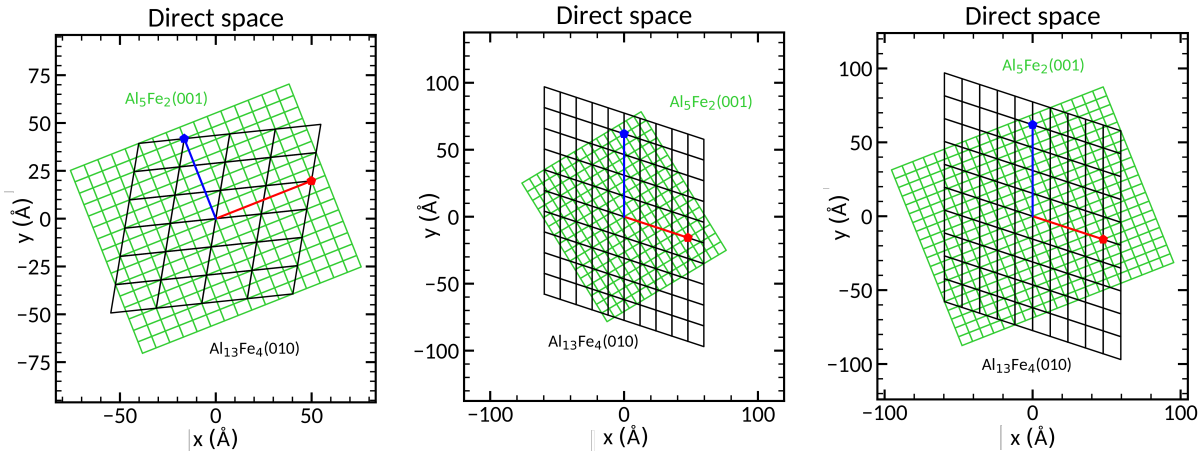

Figure 7: Scheme of the epitaxial relationships for the Vac2-2x and NVac2-2x models (a), Vac4 and NVac4 models (b), Giant model (c). The cells of the substrates and the films are shown in green and black, respectively. The dimensions of the simulated interface are indicated by the red and blue vectors.

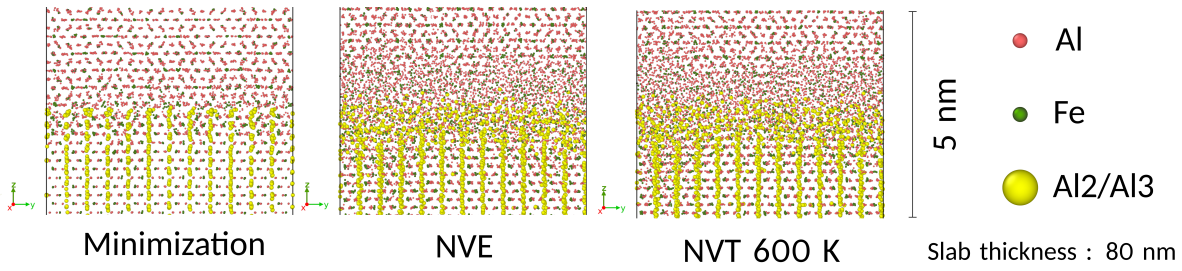

Figure 8: Snapshots of molecular dynamic simulations using the thick slab. The focus is on the Al atoms forming chains in Al_5Fe_2 (in yellow).

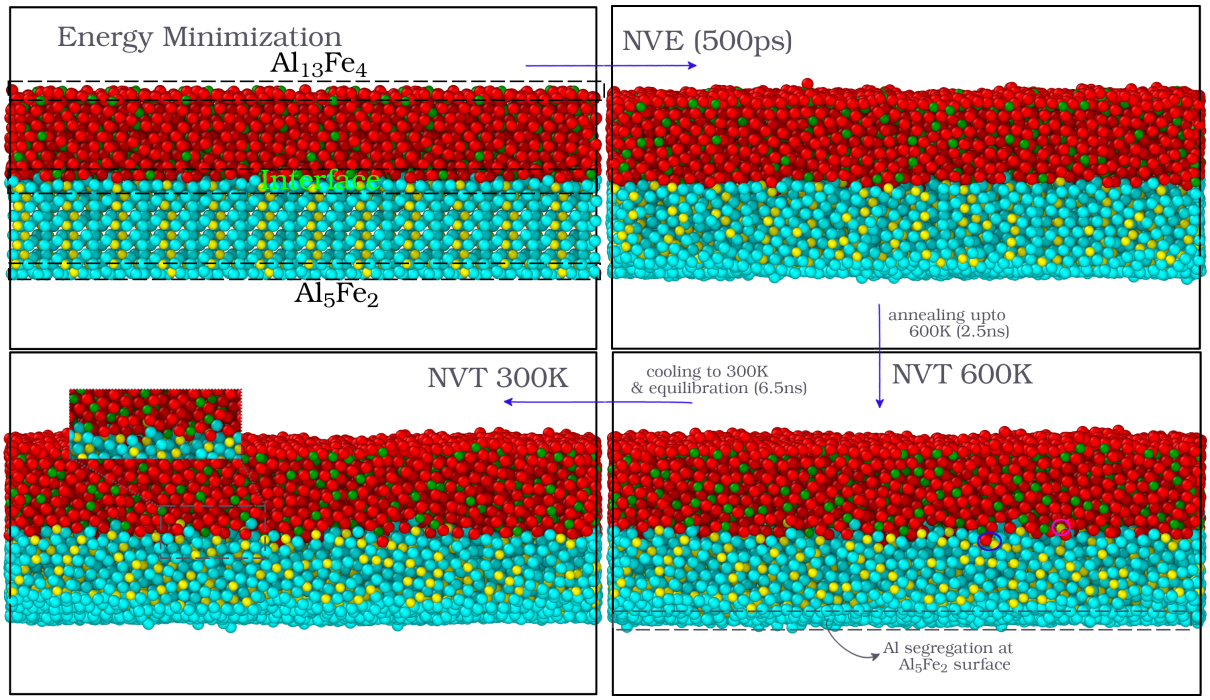

Figure 9: Snapshots of molecular dynamic simulations using the thin slab. The diffusion of Al (from $Al_{13}Fe_4$ to Al_5Fe_2) and Fe (from Al_5Fe_2 to $Al_{13}Fe_4$) is highlighted in blue and pink, respectively (at the bottom right).

Methods

Surface preparation of $Al_{13}Fe_4$(010): The experiments were performed using a single crystal ($Al_{13}Fe_4$ phase) grown by the Czochralski method and oriented using the back-scattered x-ray Laue diffraction technique. The crystal was cut parallel to the (010) plane, polished down to 0.25 μm using diamond paste and mounted onto a Ta plate. The samples were prepared by cycles of 30 min 2 keV Ar^+ sputtering followed by 1 hour annealing at 873 K under UHV conditions. The temperature is measured using an infrared optical pyrometer (emissivity set to 0.35). Neither oxygen, nor carbon surface contaminations were observed by AES prior to LEED analysis (Fig. S4).

Surface X-ray diffraction: Surface diffraction measurements were performed at the Surfaces and Interfaces X-ray Scattering (SixS) beamline at SOLEIL Synchrotron. In SixS' setup, a UHV (low 10^{-10} mbar) preparation chamber (LEED, AES) is connected to a UHV measurement chamber, mounted on a Z-axis diffractometer[49,50] allowing the transfer of the sample into the diffraction chamber. SXRD measurements were carried out at an energy of 18.41 keV and an incident angle of $\mu = 0.3^\circ$. A 2D hybrid pixel detector (XPAD S140) was used to collect the scattered intensities[51] and BINoculars program has been used to process the whole data set.[52]

AVE and ROD softwares (from the ANAROD suite[53]) were used to analyze the processed data generated by BINoculars. Several crystal truncation rods (CTRs) have been measured. Structure factors of CTRs were simulated from – in our case – DFT-relaxed surface models. The adequacy of the simulated CTRs intensities with the experimental data is quantified by the χ^2 factor

$$\chi^2 = \frac{1}{N_{data} - N_p} \sum \left| \frac{I_{exp} - I_{th}}{\sigma} \right|^2 \qquad (6)$$

where N_{data} is the number of data points, I_{exp} (resp. I_{th}) the experimental intensity (resp. simulated intensity), N_p the number of refined parameters and σ the estimated error bars. In our

Theoretical modeling Electronic structure calculations were performed with the plane wave Vienna ab initio simulation package (VASP),[54–57] using the projector augmented wave (PAW) method[58,59] and the generalized gradient approximation (GGA-PBE).[60,61] Eight valence electrons were explicitly treated for Fe ($4s^1 3d^7$) and three for Al ($3s^2 3p^1$). Total energies were minimized until the energy

differences became less than 10^{-5} eV between two electronic cycles during the structural optimizations. Atomic structures were relaxed till the Hellmann-Feynman forces were as low as 0.04 eV/Å and 0.02 eV/Å for surface and interface calculations, respectively. They were plotted using the VESTA software.[62] Calculations have been performed using a 450 eV / 350 eV energy cut-off, for the surface and interface calculations, respectively. The Brillouin zones of the different systems were sampled with Γ-centered Monkhorst-Pack k-point meshes. Only one k-point has been used for the calculations with the Giant model. Spin polarization was not taken into account since it has been shown to be not required for such an Al-rich intermetallics.[63]

The $Al_{13}Fe_4(010)$ surface was modeled with asymmetric slabs, separated by a void thickness larger than 15 Å. Surface energies were computed as a function of the Al chemical potential (see ref.[64] for the method). Interfacial energies were computed by

$$\gamma_{\text{int}} = \frac{\text{E}^{\text{tot}}_{\text{system}} - \gamma^{\text{surf}} \times \text{A} - \Sigma_{\text{x}} \text{n}_{\text{x}} \mu_{\text{x}}}{\text{A}} \qquad (7)$$

where A is the area of the interface, $\gamma^{\text{surf}} = (\gamma_{Al_5Fe_2(001)} + \gamma_{Al_{13}Fe_4(010)})$ is the sum of the non-strained surface energies of $Al_5Fe_2(001)$ and $Al_{13}Fe_4(010)$ respectively (Fig. 5, Ref.[43] and S7), n_X is the number of atoms (X species) in the computational box and μ_x their chemical potential. The latter have been set by considering $\mu_{Al} = \mu_{Al}^{\text{fcc Al}}$ and $13\mu_{Al} + 4\mu_{Fe} = \mu_{Al_{13}Fe_4}$, consistent with the fact that the $Al_{13}Fe_4$ phase first forms at the interface. Works of adhesion were computed by

$$W_{\text{adh}} = \gamma - \gamma_{\text{int}} \qquad (8)$$

with $\gamma = \gamma^{Al_5Fe_2(001)}_{\text{bulk-terminated}} + \gamma^{Al_{13}Fe_4(010)}_{Y}$ is the sum of bulk truncated surface energies (section S7). The label Y points the termination plane, i.e. $Y \in \{F, P\}$. We evaluated the constrained energy using adhesion energies:

$$\Delta \text{E}^{\text{constrain}}_{\text{film}} = \text{E}^{\text{adh}}_{\text{film}}(\text{free}) - \text{E}^{\text{adh}}_{\text{film}}(\text{contrained}) \qquad (9)$$

In the previous equation, $\text{E}^{\text{adh}}_{\text{film}}$ is the adhesion energy defined by

$$\text{E}^{\text{adh}}_{\text{film}} = \text{E}_{\text{tot}} - \text{E}_{\text{film}} - \text{E}_{\text{substrate}} \qquad (10)$$

where the film is constrained by the substrate or free.

Atomistic modeling based on pair potentials was performed using the LAMMPS molecular dynamics simulator and the MEAM interatomic potentials set by ref.[65] These potentials lead to cohesive energies for fcc Al and bcc Fe in agreement with DFT results (Tab. SS1). Moreover, negative formation enthalpies are calculated for bulk AlFe, Al_5Fe_2 and $Al_{13}Fe_4$, in agreement with the stability of these compounds (Tab. S2). Energy minimization was performed using first steep-decent algorithm followed by conjugate-gradient type. A time step of 0.5 fs was chosen during the dynamic run. The simulation box has been equilibrated sing a NVE run for 50 ps. Then, the Nose-Hoove thermostating was used in NVT run to execute simulated annealing - cooling cycle. Temperature was increased from 250 to 600 K with gradual gradient of 50K and 250ps. During the cooling cycle, the same temperature and time gradient was maintained with the last run being performed at room temperature. It was followed by another 2 ns NVT run at 300K for well-equilibration of the system.

Acknowledgment

This work is supported by the European Integrated Center for the Development of New Metallic Alloys and Compounds. C.C. acknowledges Synchrotron SOLEIL and Région Grand Est for financial support. E.G. acknowledge financial support through the COMETE project (COnception in silico de Matériaux pour l'EnvironnemenT et l'Énergie) co-funded by the European Union under the program *F*EDER-FSE Lorraine et Massif des Vosges 2014-2020. This work was granted access to the HPC resources of TGCC, CINES and IDRIS under the allocation 99642 attributed by GENCI (Grand Equipement National de Calcul Intensif). High Performance Computing resources were also partially provided by the EXPLOR centre hosted by the University de Lorraine (project 2017M4XXX0108).

Supporting Information Available

Cohesive energies, Formation enthalpies and cell parameters for fcc Al, bcc Fe, AlFe, $Al_{13}Fe_4$, Al_5Fe_2 ; SXRD reciprocal space maps, SXRD CTRs and SXRD diffraction fits ; LEED ; Structural models and epitaxial relationships ; Adhesion and interface energies of several interface models ; Surface energies

Table of Contents Graphic

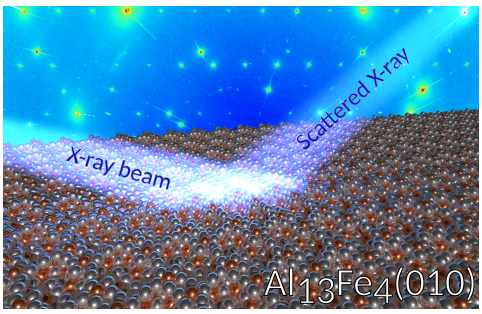

References

(1) Smirnov, E.; Peljo, P.; Scanlon, M. D.; Girault, H. H. Interfacial Redox Catalysis on Gold Nanofilms at Soft Interfaces. **2015**, *9*, 6565–6575.

(2) Song, H. C.; Lee, G. R.; Jeon, K.; Lee, H.; Lee, S. W.; Jung, Y. S.; Park, J. Y. Engineering Nanoscale Interfaces of Metal/Oxide Nanowires to Control Catalytic Activity. *ACS Nano* **2020**, *14*, 8335–8342.

(3) Xie, C.; Niu, Z.; Kim, D.; Li, M.; Yang, P. Surface and Interface Control in Nanoparticle Catalysis. *Chem. Rev.* **2020**, *120*, 1184–1249.

(4) Feng, M.; Feng, Y.; Zhang, T.; Li, J.; Chen, Q.; Chi, Q.; Lei, Q. Recent Advances in Multilayer-Structure Dielectrics for Energy Storage Application. *Adv. Sci.* **2021**, *8*, 2102221.

(5) Huang, Z.; Ariando,; Renshaw-Wang, X.; Rusydi, A.; Chen, J.; Yang, H.; Venkatesan, T. Interface Engineering and Emergent Phenomena in Oxide Heterostructures. *Adv. Mater.* **2018**, 1802439.

(6) Montemor, M. Functional and Smart Coatings for Corrosion Protection: a Review of Recent Advances. *Surface and Coatings Technology* **2014**, *258*, 17–37.

(7) R.M.Fillion,; A.R.Riahi,; A.Edrisy, A Review of Icing Prevention in Photovoltaic Devices by Surface Engineering. *Renewable and Sustainable Energy Reviews* **2014**, *32*, 797–809.

(8) Attarzadeh, N.; Molaei, M.; Babaei, K.; Fattah-alhosseini, A. New Promising Ceramic Coatings for Corrosion and Wear Protection of Steels: A Review. *Surfaces and Interfaces* **2021**, *23*, 100997.

(9) Kidson, G. Some Aspects of the Growth of Diffusion Layers in Binary Systems. *Journal of Nuclear Materials* **1961**, *3*, 21–29.

(10) Carvalho, G.; I.Galvao,; R.Mendes,; R.M.Leal,; A.Loureiro, Microstructure and Mechanical Behaviour of Aluminium-Carbon Steel and Aluminium-Stainless Steel Clads Produced with an Aluminium Interlayer. *Materials Characterization* **2019**, *155*, 109819.

(11) Kobayashi, S.; Yakou, T. Control of Intermetallic Compound Layers at Interface between Steel and Aluminum by Diffusion-Treatment. *Materials Science and Engineering: A* **2002**, *338*, 44–53.

(12) Shang, S.; Sun, H.; Pan, B.; Krajewski, A. M.; Banu, M.; Li, J.; Liu, Z.-K. Forming Mechanism of Equilibrium and Non-Equilibrium Metallurgical Phases in Dissimilar Aluminum/Steel (AlFe) Joints. *Sci Rep* **2021**, *11*, 24251.

(13) Lotfian, S.; Rolink, G.; Weisheit, A.; Palm, M. Chemically Graded Fe-Al/Steel Samples Fabricated by Laser Metal Deposition. **2017**, *2*, 1393.

(14) Hussein, S.; Tahir, A.; Hadzley, A. Characteristics of Aluminum-to-Steel Joint Made by Friction Stir Welding: A Review. **2015**, *5*, 32.

(15) Shen, C.; Pan, Z.; Ma, Y.; Cuiuri, D.; Li, H. Fabrication of Iron-Rich Fe-Al Intermetallics using the Wire-Arc Additive Manufacturing Process. *Addit. Manuf.* **2015**, *7*, 20.

(16) Shen, C.; Pan, Z.; Cuiuri, D.; Roberts, J.; Li, H. Fabrication of Fe-FeAl Functionally Graded Material Using the Wire-Arc Additive Manufacturing Process. *Metall. Mater. Trans. B* **2016**, *47*, 763.

(17) Shakiba, M.; Parson, N.; Chen, X.-G. Effect of Homogenization Treatment and Silicon Content on the Microstructure and Hot Workability of Dilute Al-Fe-Si Alloys. *Materials Science and Engineering: A* **2014**, *619*, 180189.

(18) Alexander, W.; Slifkin, L. Diffusion of Solutes in Aluminum and Dilute Aluminum Alloys. *Phys. Rev. B* **1970**, *1*, 3274.

(19) Zhang, G.; Chen, M.; Shi, Y.; Huang, J.; Yang, F. Analysis and Modeling of the Growth of Intermetallic Compounds in Aluminum-Steel Joints. *RSC Adv.* **2017**, *7*, 37797.

(20) He, H.; Gou, W.; Wang, S.; Hou, Y.; Ma, C.; Mendez, P. F. Kinetics of Intermetallic Compound Layers during Initial Period of Reaction between Mild Steel and Molten Aluminum. *Int. J. Mater. Res.* **2019**, *110*, 194.

(21) Wang, H.; Yang, F.; Zhang, Z.; Liu, L. Bonding Mechanism of Al/Steel Interface Formed by Laser-TIG Welding Assisted Riveting Technology. *Mater. Today Commun.* **2020**, *25*, 101487.

(22) Mendelev, M. I.; Srolovitz, D. J.; Ackland, G. J.; Han, S. Effect of Fe Segregation on the Migration of a Non-Symmetric $\Sigma5$ Tilt Grain Boundary in Al. *Journal of Materials Research* **2005**, *20*, 208–218.

(23) Zhang, C.-H.; Huang, S.; Shen, J.; Chen, N.-X. Structural and Mechanical Properties of Fe-Al Compounds: An Atomistic Study by EAM Simulation. *Intermetallics* **2014**, *52*, 86–91.

(24) Lee, E.; Lee, B.-J. Modified Embedded-Atom Method Interatomic Potential for the FeAl System. *J. Phys.: Condens. Matter* **2010**, *22*, 175702.

(25) Jelinek, B.; Groh, S.; Horstemeyer, M. F.; Houze, J.; Kim, S. G.; Wagner, G. J.; Moitra, A.; Baskes, M. I. Modified Embedded Atom Method Potential for Al, Si, Mg, Cu, and Fe Alloys. *Phys. Rev. B* **2012**, *85*, 245102.

(26) Sakidja, R.; Perepezko, J.; Calhoun, P. Synthesis, Thermodynamic Stability and Diffusion Mechanism of Al_5Fe_2-Based Coatings. *Oxidation of Metals* **2014**, *81*, 167–177.

(27) Fang, C. M.; Dinsdale, A.; Que, Z. P.; Fan, Z. Intrinsic Defects in and Electronic Properties of θ-$Al_{13}Fe_4$: an Ab Initio DFT Study. *J. Phys. Mater.* **2019**, *2*, 015004.

(28) Scheid, P.; Chatelier, C.; Ledieu, J.; Fournée, V.; Gaudry, E. Bonding Network and Stability of Clusters: The Case Study of the $Al_{13}TM_4$ Pseudo-10fold Surfaces. *Acta Crystallogr. A* **2019**, *75*, 314–324.

(29) El-Chlouk, Z.; Kassem, W.; Shehadeh, M.; Hamade, R. F. On the Mechanical Response and Intermetallic Compound Formation in Al/Fe Interface: Molecular Dynamics Analyses. *Philosophical Magazine* **2020**, *100*, 3041–3060.

(30) Khalid, M. Z.; Friis, J.; Ninive, P. H.; Marthinsen, K.; Strandlie, A. Ab-initio Study of Atomic Structure and Mechanical Behaviour of Al / Fe Intermetallic Interfaces. *Computational Materials Science* **2020**, *174*, 109481.

(31) Khalid, M. Z.; Friis, J.; Ninive, P. H.; Marthinsen, K.; Strandlie, A. First-Principles Sudy of Tensile and Shear Strength of Fe-Al and α-AlFeSi Intermetallic Compound Interfaces. *Computational Materials Science* **2021**, *187*, 110058.

(32) Khalid, M. Z.; Friis, J.; Ninive, P. H.; Marthinsen, K.; Strandlie, A. First-Principles Study of Tensile and Shear Strength of an Fe_2Al_5//Fe Interface. *Computational Materials Science* **2021**, *192*, 110319.

(33) Stradi, D.; Jelver, L.; Smidstrup, S.; Stokbro, K. Method for Determining Optimal Supercell Representation of Interfaces. *J. Phys. Condens. Matter* **2017**, *29*, 185901.

(34) Grin, J.; Burkhardt, U.; Ellner, M.; Peters, K. Refinement of the Fe_4Al_{13} Structure and its Relationship to the Quasi-homological Homeotypical Structures. *Z. Kristallogr.* **1994**, *209*, 479–487.

(35) Schubert, K.; Rösler, U.; Kluge, M.; Anderko, K.; Härle, L. Kristallographische Ergebnisse an Phasen mit Durchdringungsbindung. *Naturwissenschaften* **1953**, *40*, 437.

(36) Burkhardt, U.; Grin, Y.; Ellner, M.; Peters, K. Structure Refinement of the Iron-Aluminium Phase with the Approximate Composition Al_5Fe_2. *Acta Crystallogr.* **1994**, *B50*, 313–316.

(37) Ellner, M.; Mayer, J. X-ray and Electron Diffraction Investigations of the Liquid-Quenched Fe_2Al_5. *Scr. Metall. Mater.* **1992**, *26*, 501–504.

(38) Black, P. The Structure of $FeAl_3$. *Acta Crystallographica* **1955**, *8*, 43–48.

(39) Henley, C. L. Current Models of Decagonal Atomic Structure. *J. Non-Cryst. Solids* **1993**, *153-154*, 172.

(40) Balluffi, R. W. Vacancy Defect Mobilities and Binding Energies Obtained from Annealing Studies. *J. Nucl. Mater.* **1978**, *69-70*, 240–263.

(41) Ledieu, J.; Gaudry, E.; Loli, L. N. S.; Villaseca, S. A.; de Weerd, M.-C.; Hahne, M.; Gille, P.; Grin, Y.; Dubois, J.-M.; Fournée, V. Structural Investigation of the (010) Surface of the $Al_{13}Fe_4$ Catalyst. *Phys. Rev. Lett.* **2013**, *110*, 076102.

(42) Matilainen, A.; Pussi, K.; Diehl, R. D.; Ledieu, J.; Hahne, M.; Gille, P.; Gaudry, .; Loli, L. S.; McGuirk, G.; de Weerd, M.-C.; Fournée, V.; Ledieu, J. Structure of the Monoclinic $Al_{13}Fe_4$(010) Complex Metallic Alloy Surface Determined by Low-Energy Electron Diffraction. *Phys. Rev. B* **2015**, *92*, 014109.

(43) Boulley, L.; Kandaskalov, D.; de Weerd, M.-C.; Migot, S.; Ghanbaja, J.; Sturm, S.; Boulet, P.; Ledieu, J.; Gaudry, E.; Fournée, V. Investigation of the (100) and (001) Surfaces of the Al_5Fe_2 Intermetallic Compound. *Applied Surface Science* **2021**, *542*, 148540.

(44) Zur, A.; McGill, T. Lattice Match: an Application to Heteroepitaxy. *J. Appl. Phys.* **1984**, *55*, 378–386.

(45) Mathew, K.; Gabriel, J. J.; Ashton, M.; Singh, A. K.; Paul, J. T.; Kolluru, V. S. C.; Monahan, S. G.; Hennig, R. G. MPInterfaces - Python Package for High Throughput Analysis of Materials Interfaces. `https://github.com/henniggroup/MPInterfaces`, 2018; `https://github.com/henniggroup/MPInterfaces`.

(46) Mathew, K.; Singh, A. K.; Gabriel, J. J.; Choudhary, K.; Sinnott, S. B.; Davydov, A. V.; Tavazza, F.; Hennig, R. G. MPInterfaces: A Materials Project Based Python Tool for High-Throughput Computational Screening of Interfacial Systems. *Comp. Mater. Sci.* **2016**, *122*, 183 – 190.

(47) Khalid, M. Z.; Friis, J.; Ninive, P. H.; Marthinsen, K.; Strandlie, A. DFT Calculations Based Insight into Bonding Character and Strength of Fe_2Al_5 and Fe_4Al_{13} Intermetallics at Al-Fe Joints. *Procedia Manufacturing* **2018**, *15*, 1407–1415.

(48) Ju, G.; Xu, D.; Thompson, C.; Highland, M. J.; Eastman, J. A.; Walkosz, W.; Zapol, P.; Stephenson, G. B. In Situ Microbeam Surface X-ray Scattering Reveals Alternating Step Kinetics During Crystal Growth. *Nat. Commun.* **2021**, *12*, 1721.

(49) Vlieg, E. Integrated Intensities Using A Six-Circle Surface X-Ray Diffractometer. *J. Appl. Cryst* **1997**, *30*, 532–543.

(50) Robach, O.; Garreau, Y.; Aïd, K.; Véron-Jolliot, M. B. Corrections for Surface X-Ray Diffraction Measurements Using the Z-Axis Geometry: Finite Size Effects in Direct and Reciprocal Space. *J. Appl. Cryst.* **2000**, *33*, 1006–1018.

(51) Drnec, J.; Zhou, T.; Pintea, S.; Onderwaater, W.; Vlieg, E.; Renaud, G.; Felici, R. Integration Techniques for Surface

X-Ray Diffraction Data Obtained With A Two-Dimensional Detector. *J. Appl. Cryst.* **2014**, *47*, 365–377.

(52) Roobol, S.; Onderwaater, W.; Drnec, J.; Felici, R.; Frenken, J. BINoculars : Data Reduction and Analysis Software for Two-Dimensional Detectors in Surface X-Ray Diffraction. *J. Appl. Cryst.* **2015**, *48*, 1324–1329.

(53) Vlieg, E. ROD: A Program for Surface X-Ray Crystallography. *J. Appl. Cryst* **2000**, *33*, 401–405.

(54) Kresse, G.; Hafner, J. Ab Initio Molecular Dynamics for Liquid Metals. *Phys. Rev. B* **1993**, *47*, 558–561.

(55) Kresse, G.; Hafner, J. Ab Initio Molecular-Dynamics Simulation of the Liquid-Metal-Amorphous-Semiconductor Transition in Germanium. *Phys. Rev. B* **1994**, *49*, 14251–14269.

(56) Kresse, G.; Furthmüller, J. Efficient Iterative Schemes for Ab Initio Total-Energy Calculations Using A Plane-Wave Basis Set. *Phys. Rev. B* **1996**, *54*, 11169 – 11186.

(57) Kresse, G.; Furthmüller, J. Efficiency of Ab-Initio Total Energy Calculations For Metals and Semiconductors Using a Plane Wave Basis Set. *Comput. Mater. Sci.* **1996**, *6*, 15–50.

(58) Blochl, P. E. Projector Augmented-Wave Method. *Phys. Rev. B* **1994**, *50*, 17953–17979.

(59) Kresse, G.; Joubert, D. From Ultrasoft Pseudopotentials To the Projector Augmented-Wave Method. *Phys. Rev. B* **1999**, *59*, 1758–1775.

(60) Perdew, J. P.; Burke, K.; Ernzerhof, M. Generalized Gradient Approximation Made Simple . *Phys. Rev. Lett.* **1996**, *77*, 3865.

(61) Perdew, J. P.; Burke, K.; Ernzerhof, M. Erratum: Generalized Gradient Approximation Made Simple. *Phys. Rev. Lett.* **1997**, *78*, 1396.

(62) Momma, K.; Izumi, F. VESTA 3 for Three-Dimensional Visualization of Crystal, Volumetric and Morphology Data. *J. Appl. Crystallogr.* **2011**, *44*, 1272–1276.

(63) Mihalkovic, M.; Widom, M. Structure and Stability of Al_2Fe and Al_5Fe_2: First-Principles Total Energy and Phonon Calculations. *Physical Review B* **2012**, *85*, 014113.

(64) Reedijk, J., Poeppelmeier, K., Eds. *Comprehensive Inorganic Chemistry III*; Springer: Berlin, 2022.

(65) Lee, K.; Morikawa, Y.; Langreth, D. C. Adsorption of n-butane on Cu(100), Cu(111), Au(111), and Pt(111): Van der Waals density-functional study. *Phys. Rev. B* **2010**, *82*, 155461.